

Article

High-Throughput Preparation and Mechanical Property Screening of Zr-Ti-Nb-Ta Multi-Principal Element Alloys via Multi-Target Sputtering

Haochen Qiu^{1,2}, Xuehui Yan^{1,2}, Shuaishuai Wu^{1,2}, Wei Jiang^{1,2}, Baohong Zhu^{1,2,*} and Shengli Guo^{1,2}

¹ GRIMAT Engineering Institute Co., Ltd., Beijing 101400, China; qiuhaochen@grinm.com (H.Q.); yanxh_ustb@163.com (X.Y.); wushuaishuai@grinm.com (S.W.); jiangwei@grinm.com (W.J.); guoshengli@grinm.com (S.G.)

² China GRINM Group Corporation Limited, Beijing 100088, China

* Correspondence: zhubaohong@grinm.com

Abstract: Zr-Ti-Nb-Ta alloys were synthesized in parallel via multi-target co-sputtering deposition with physical masking in a pseudo-ternary Ti-Nb-ZrTa alloy system. Sixteen alloys with distinct compositions were obtained. Comprehensive characterization of phase structure, microstructure, Young's modulus, and nanoindentation hardness was undertaken. The Ti-Nb-ZrTa alloys exhibited two typical phase structures: a single-BCC solid-solution structure, and an amorphous structure. Nanoindentation quantification confirmed a Young's modulus ranging from 110 to 130 GPa, alongside nanoindentation hardness spanning 3.6 to 5.0 GPa. The combination of good hardness and a relatively low Young's modulus renders these alloys promising candidates for excellent biomedical materials. This work not only offers an effective method for the high-throughput synthesis of multi-principal element alloys, but also sheds light on a strategy for screening the phase structure and mechanical performance within a given alloy system.

Keywords: high-throughput preparation; phase structure; microstructure; Young's modulus; nanoindentation hardness



Citation: Qiu, H.; Yan, X.; Wu, S.; Jiang, W.; Zhu, B.; Guo, S.

High-Throughput Preparation and Mechanical Property Screening of Zr-Ti-Nb-Ta Multi-Principal Element Alloys via Multi-Target Sputtering. *Coatings* **2023**, *13*, 1650. <https://doi.org/10.3390/coatings13091650>

Academic Editor: Hideyuki Murakami

Received: 9 August 2023

Revised: 4 September 2023

Accepted: 8 September 2023

Published: 20 September 2023



Copyright: © 2023 by the authors. Licensee MDPI, Basel, Switzerland. This article is an open access article distributed under the terms and conditions of the Creative Commons Attribution (CC BY) license (<https://creativecommons.org/licenses/by/4.0/>).

1. Introduction

Multi-principal element alloys (MPEAs) are a novel class of materials obtained via designing chemical disorders at the atomic scale [1]. Unlike traditional alloys, whose performance is designed with a dominant element and fewer additional elements in mind, MPEAs generally contain several dominant elements (no less than three), aiming to demonstrate unique mechanical, physical, and chemical properties in a wider composition space [2]. MPEAs usually cover the fields of medium-entropy alloys and high-entropy alloys. Many excellent properties have been proved in MPEAs, such as breaking the trade-off between strength and ductility [3–5], good thermal stability [6,7], excellent low-temperature ductility [8,9], outstanding corrosion resistance [10–12] and irradiation resistance [13–15], etc. The complex compositions of MPEAs enable these advantages, but also make alloys' design and property prediction more challenging than for traditional alloys. High-throughput preparation and screening of MPEAs can thus improve design efficiency [16–18].

At present, many efforts have focused on the Zr-Ti-Nb-Ta alloy system. Several Zr-Ti-Nb-Ta alloys are considered ideal structural materials due to their high strength and excellent plastic deformation capacity [19–22]. For example, $Ti_{45}Zr_{45}Nb_5Ta_x$ ($x = 5, 10, 15$ at. %) alloys with a single-BCC structure showed outstanding tensile ductility (~20%) and high tensile strength (800–1200 MPa) [22]. However, a wide composition space remains unexplored. In general, the reported alloy composition is randomly matched, or only a few composition content variables are set. In this case, besides the reported composition, there may be other optimal compositions of this alloy system that have not been explored. If we can screen the

properties within a wider composition space, the results will be more convincing. Multi-target co-sputtering combined with a shielding mask offers a flexible high-throughput preparation method, which has been applied to many MPEAs systems, including Al-Cr-Fe-Ni-Ti [16], Zr-Ti-Nb [17], and Cr-Fe-V-Ta-W [18] alloy systems, to screen disordered alloy composition, phase structure, mechanical properties, and photothermal absorption ability.

The purpose of this work is to provide effective parallel preparation methods of multi-principal element alloys in a pseudo-ternary Ti-Nb-Zr-Ta system. Multi-target co-sputtering with a physical mask was used to prepare 16 independent Ti-Nb-Zr-Ta alloys with different compositions. Based on the composition library developed for the Zr-Ti-Nb-Ta system, the relationship between phase structure, microstructure, and mechanical properties, as well as the trends in mechanical properties, were studied and preliminarily screened.

2. Materials and Methods

Parallel Preparation

The method of combining co-sputtering deposition with physical masking was applied to the parallel preparation of the Ti-Nb-Zr-Ta alloy system. The targets were classified into a ZrTa alloy target, a pure Ti target, and a pure Nb target (all elements with a purity > 99.9 wt.%). It should be noted that the composition ratio of ZrTa is 1:1. The three targets were 120° apart from each other, and all of them focused on the substrate; the schematic diagrams are shown in Figure 1. Differing from conventional co-sputtering, where the substrate rotates at a certain rate, the substrate in this work is stable. In this case, the differing relative positions between the target materials and substrate induce spatial variations in deposition density, yielding a compositionally graded film on the substrate. To preclude interdiffusion during deposition, a mask was utilized to shield the substrate. Each sample had a square geometry with dimensions of 10 mm × 10 mm. In one deposition, 16 distinct composition samples were synthesized and arranged in a matrix array on the substrate, as depicted in Figure 1. For unambiguous sample identification, an A-B naming convention was adopted, where A denotes the vertical axis number and B denotes the horizontal axis number (A ranges from 1 to 4, and B ranges from 1 to 4), as delineated in Figure 1.

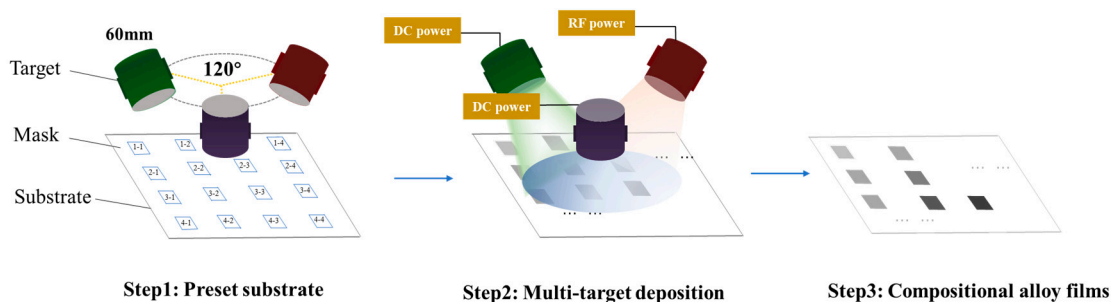
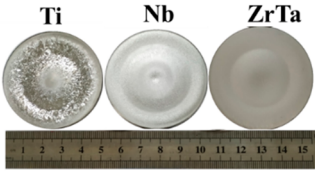


Figure 1. Schematic diagram of high-throughput preparation via a multi-target co-sputtering method.

All of these targets with a diameter of 50 mm and a thickness of 3 mm were fabricated via a hot-pressing process. The ZrTa alloy target was mounted on a direct current (DC) power supply at a power of 80 W. The Ti target was also mounted on a DC power supply at a power of 100 W. The Nb target was mounted on a (radio frequency) RF power supply with a power of 80 W. The specific working parameters and physical pictures of targets are listed in Table 1. A P-type Si (100) wafer covered with a 300 nm silicon-oxide coating was selected as a substrate for this work. The wafer was disc-shaped, with a diameter of 15.24 cm and with a thickness of 625 μm. Before the co-deposition, the base pressure was maintained at 5×10^{-4} Pa. Then, high-purity argon was induced into the vacuum chamber, and targets underwent pre-sputtering cleaning for 15 min. Critically, the baffles above the targets were blocked during this process. Finally, co-sputtering commenced, fabricating the “materials library”. It should be noted that the Nb element is a positive element to

the stable β phase, which is expected to maintain a relatively moderate level of element content. Hence, the Nb target is the equipment on the RF power supply.

Table 1. The working conditions and physical pictures of targets.

Target	Powder Type	Powder Parameter	Target Pictures
Ti	DC	100 W	
Nb	RF	80 W	
ZrTa	DC	80 W	

The surface morphology and cross-sectional microstructure of alloy films were characterized via field-emission scanning electron microscopy (SEM) (Auriga Field Emission Scanning Electron Microscope, Carl Zeiss, Jena, Germany). The chemical composition was analyzed with an SEM device equipped with an energy-dispersive X-ray spectrometer (EDX). The phase structure of samples was tested with an X-ray diffractometer (XRD, BRUKERD8 Discover, Bruker, Karlsruhe, Germany), using Cu $K\alpha$ radiation with a scanning range was 20° – 90° . It should be noted that the small-angle X-ray scattering (SAXS) technique was used in this work, and the scanning rate was about 4° /min. The mechanical properties were mainly focused on the nanoindentation hardness and Young's modulus of samples, which were tested using a nanoindenter and a Berkovich triangular pyramid indenter (OLS-4100, Olympus, Tokyo, Japan). Each sample was tested at least five points at different places, and the distance between each indentation was $50\ \mu\text{m}$. To avoid the effect of the substrate, the maximum pressing depth for testing hardness was $500\ \text{nm}$.

3. Results

3.1. Composition Analysis of Ti-Zr-Nb-Ta Material Library

As characterized by EDX analysis, the final chemical compositions of the sixteen samples are shown in Table 2. It was found that the content of the Ti ranges from 13 at. % to 71 at. %, the content of the Zr element ranges from 14 at. % to 47 at. %, the content of the Nb element ranges from 7 at. % to 43 at. %, and the content of the Ta element ranges from 7 at. % to 28 at. %. A pseudo-ternary component phase diagram is presented in Figure 2, along with a schematic diagram describing the relative positions of the targets and 16 samples. Notably, the compositional analysis revealed that proximity to a given target resulted in a higher proportion of that target material. Conversely, as the distance from a given target increased, its proportional composition decreased. The mixing entropies of Ti-Zr-Nb-Ta alloys were calculated by the following equation, which is described according to Boltzmann's hypothesis [23]:

$$\Delta S_{mix} = -R \sum_{i=1}^n c_i \ln c_i$$

where R is the gas constant ($R = 8.314\ \text{J}/(\text{K}\cdot\text{mol})$), and c_i is the mole percent of a certain component, hence the $\sum_i^n c_i$ equals 1. The calculation results show that the mixing entropy of these Ti-Zr-Nb-Ta alloys ranges from $0.9R$ to $1.36R$. In this case, these multi-component alloys mainly belong to medium-entropy alloys.

Table 2. Chemical compositions of Ti-Zr-Nb-Ta alloy system.

Number	Ti	Zr	Nb	Ta	Composition
1-1	71.22	14.14	6.61	7.28	Ti ₇₁ Zr ₁₄ Nb ₇ Ta ₇
1-2	57.46	17.92	15.00	9.62	Ti ₅₇ Zr ₁₈ Nb ₁₅ Ta ₁₀
1-3	39.84	20.12	29.26	10.78	Ti ₄₀ Zr ₂₀ Nb ₂₉ Ta ₁₁
1-4	26.10	20.26	43.05	10.59	Ti ₂₆ Zr ₂₀ Nb ₄₃ Ta ₁₁
2-1	62.01	19.90	7.72	10.37	Ti ₆₂ Zr ₂₀ Nb ₈ Ta ₁₀
2-2	48.04	24.45	14.35	13.16	Ti ₄₈ Zr ₂₅ Nb ₁₄ Ta ₁₃
2-3	33.74	28.84	22.00	15.41	Ti ₃₄ Zr ₂₉ Nb ₂₂ Ta ₁₅
2-4	23.89	28.15	32.10	15.86	Ti ₂₄ Zr ₂₈ Nb ₃₂ Ta ₁₆
3-1	44.80	31.10	7.60	16.50	Ti ₄₅ Zr ₃₁ Nb ₈ Ta ₁₆
3-2	34.80	34.98	10.46	19.76	Ti ₃₅ Zr ₃₅ Nb ₁₀ Ta ₂₀
3-3	27.29	36.24	15.8	20.67	Ti ₂₇ Zr ₃₆ Nb ₁₆ Ta ₂₁
3-4	18.17	40.28	18.97	22.58	Ti ₁₈ Zr ₄₀ Nb ₁₉ Ta ₂₃
4-1	28.80	42.34	6.24	22.62	Ti ₃₀ Zr ₄₂ Nb ₆ Ta ₂₃
4-2	19.77	45.99	8.11	26.13	Ti ₂₀ Zr ₄₆ Nb ₈ Ta ₂₆
4-3	15.45	46.98	9.73	27.84	Ti ₁₅ Zr ₄₇ Nb ₁₀ Ta ₂₈
4-4	13.44	45.28	15.88	25.40	Ti ₁₃ Zr ₄₅ Nb ₁₆ Ta ₂₆

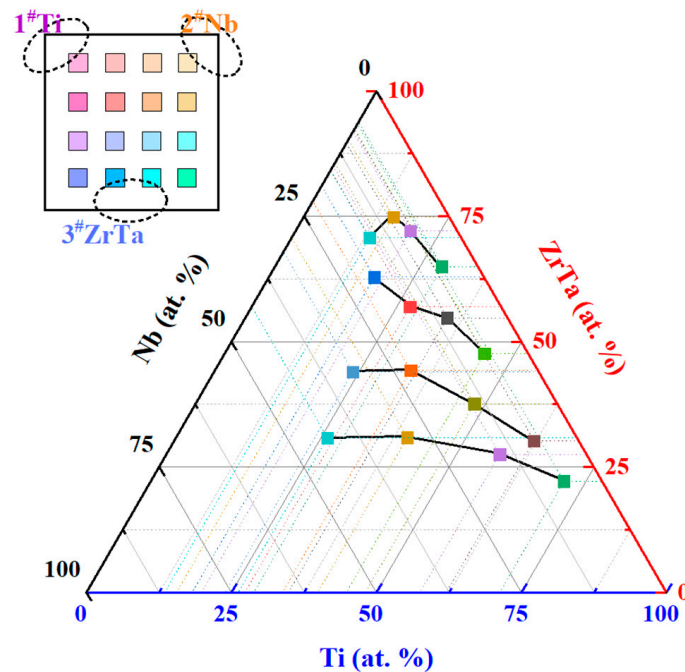


Figure 2. Location of Ti-Zr-Nb-Ta alloys in a pseudo-ternary compositional map.

As depicted in Figure 3, the variation patterns of the constituent elements were examined separately. The Zr and Ta elements were alloyed in a single target; thus, the compositional trends for Zr and Ta were consistent. As noted, the sample units were named A-B, where A denotes the horizontal serial number. It was observed that higher A values corresponded to increased ZrTa content, as the distance between the sample units and ZrTa target decreased with increasing A. Hence, the compositional variations followed a simple linear relationship correlated with the relative distance and position between the sample unit and target material. The trends in Ti and Nb content, shown in Figure 3c,d, further validated this relationship.

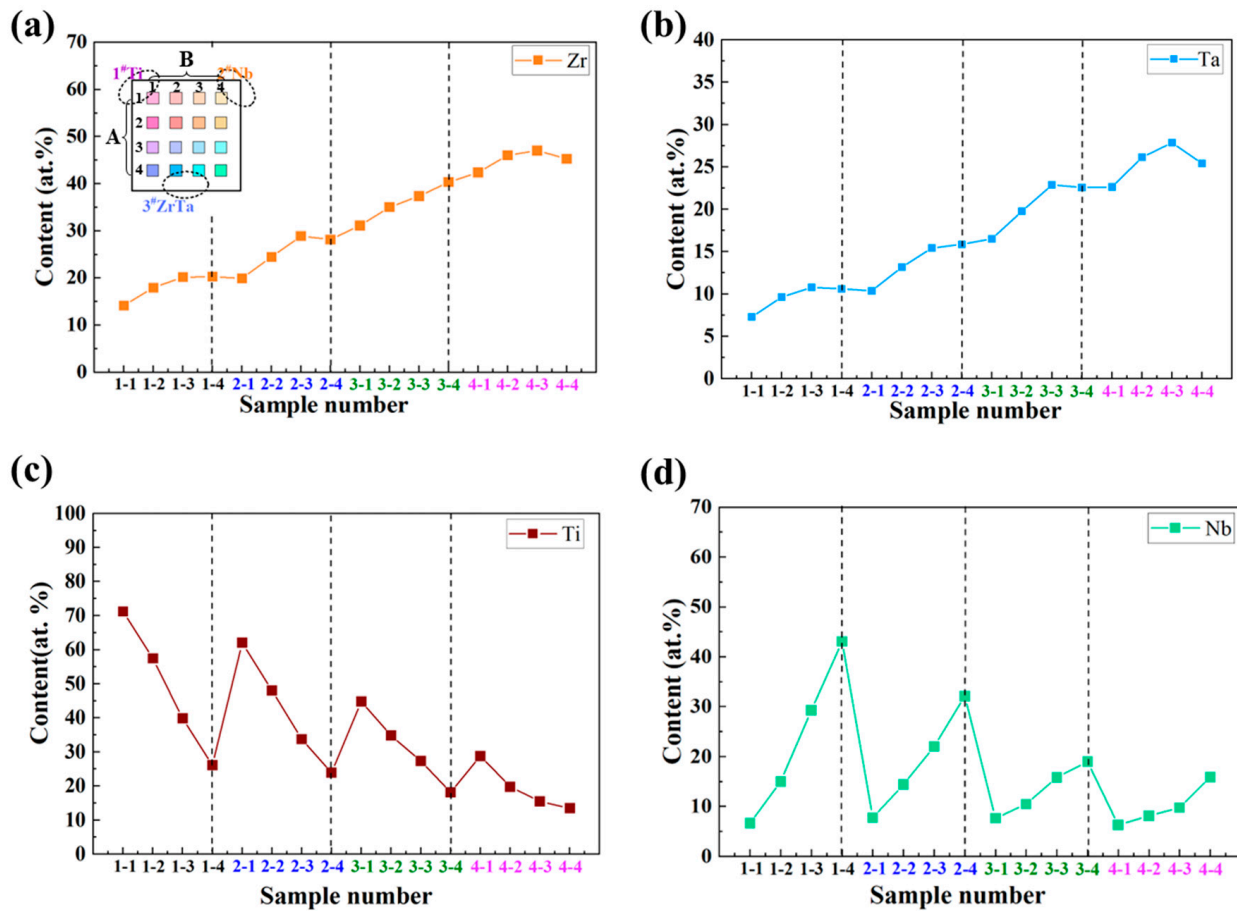


Figure 3. The law of composition changes: (a) Zr, (b) Ti, (c) Ta, and (d) Nb.

3.2. Phase Structure and Microstructure Characterization and Analysis

The phase structures of 16 Zr-Ti-Nb-Al alloys were characterized via XRD, as shown in Figure 4. Overall, these alloys show two different phase structures including a single-body-centered cubic (BCC) structure and an amorphous structure. Using an analysis of composition changes, it can be found that alloys with high ZrTa content are amorphous structures. Moreover, with the increase in the ZrTa content, the diffraction peaks shift towards a low angle, which means larger lattice parameters. Combining $d_{hkl} = \frac{a}{\sqrt{h^2+k^2+l}}$ with the Bragg diffraction formula of $2d\sin\theta = \lambda$, the lattice constant (a) is expressed as $a = \lambda\sqrt{h^2+k^2+l}/2\sin\theta$. Here, λ is the wavelength of X-ray radiation, d_{hkl} is the interplanar spacing, and θ is the diffraction angle. Typical parameters for the components are listed in Table 3. The atomic radius of Zr is larger than other components. In this case, as the content of Zr and Ta increases, the lattice constant increases, resulting in a corresponding decrease in the diffraction angles of peaks.

Table 3. The parameters of the constituent elements of Ti-Zr-Nb-Ta alloy systems.

Element	Atomic Radius r (nm)	Lattice Parameter a (nm)
Ti	0.143	0.32998
Zr	0.160	0.3609
Nb	0.143	0.33007
Ta	0.146	0.33013

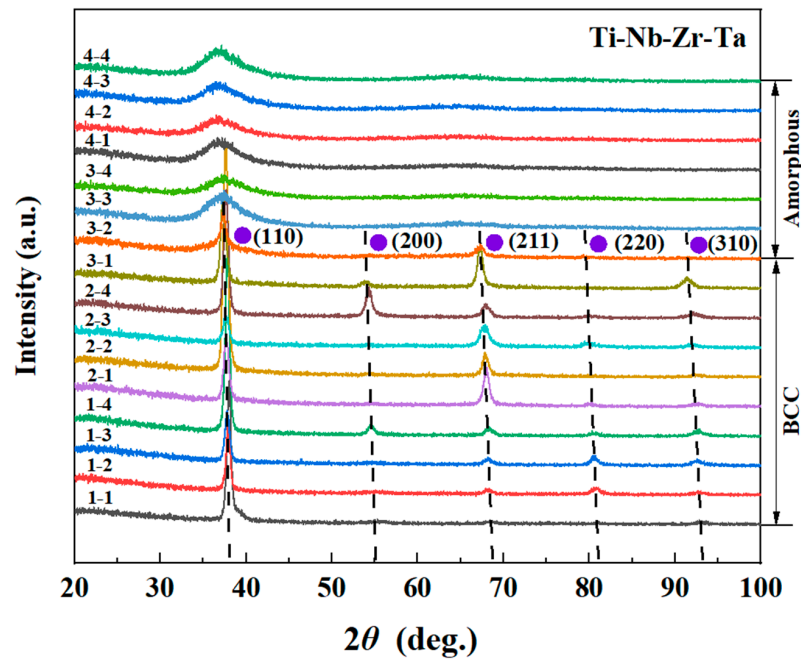


Figure 4. XRD patterns of 16 Ti-Zr-Nb-Ta alloys.

Figure 5 presents SEM images of the sixteen Ti-Zr-Nb-Ta alloys, arranged corresponding to the specimen locations on the substrate. As shown, the morphologies of the alloys somewhat varied with composition. The images can be broadly categorized into two topographic groups, delineated by colored lines: (1) a rough surface with granular features, and (2) a relatively smooth surface without particles. Combining these images with a phase structure analysis, it was found that the alloys with granular features possess a single-BCC phase structure, while the alloys with smooth surface features possess an amorphous structure. In other words, alloys with a BCC phase structure displayed distinct nanocrystalline structures, whereas amorphous alloys lacked such nanocrystalline characteristics.

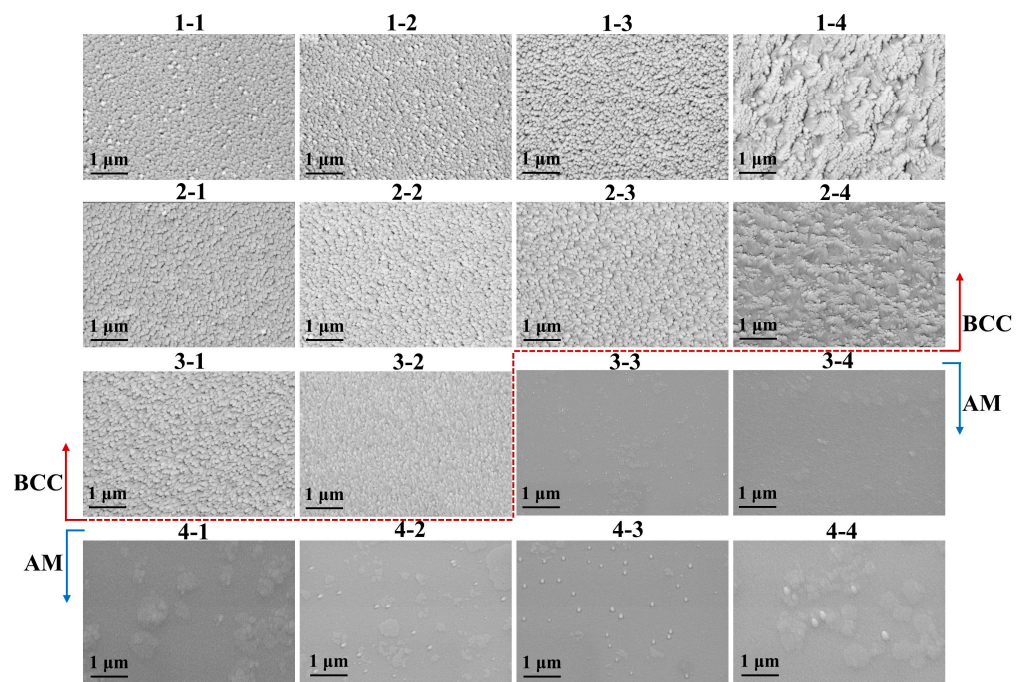


Figure 5. SEM images of the deposited Ti-Zr-Nb-Ta alloys taken from the surface.

According to the composition analysis, the amorphous alloys contain a relatively high Zr and Ta content, and possess a relatively large atomic radius. The formation of amorphous phases in several films can be rationalized in two ways: (1) the amorphous alloy films possess a high Zr and Ta content, which exacerbates the atomic size mismatch within these alloys, thereby hindering the formation of a highly crystalline structure; (2) the higher cooling rate inherent to magnetron sputtering, compared to melting methods, induces a non-equilibrium state in the sputtered films, and this further facilitates amorphous structure formation. Briefly, an increase in the atomic size mismatch will correspondingly cause an increase in atomic size strain within the HEA lattice. In this case, the instability of the lattice will be exacerbated. At the same time, with the support of a high cooling rate in the sputtering, the amorphous phase will dominate in HEA films with a high Zr content. It should be noted that the microstructure of films was significantly affected by the atomic diffusion ability. For crystal films, the lattice was in a stable state with lower lattice energy versus the metastable state. In this case, the deposited atoms for crystal films possess a stronger diffusion ability, enabling rapid surface diffusion. Consequently, the grain boundaries were mobile, imparting a granular surface morphology.

3.3. Mechanical Properties' Characterization and Analysis

The mechanical properties of Ti-Zr-Nb-Ta alloys were tested via nanoindentation, mainly focusing on the hardness and Young's modulus. For clarity, the tested indentation hardness values were compiled into contour maps, as presented in Figure 6. Overall, the hardness across the 16 specimens spanned 5 to 8.5 GPa. A region of relatively high hardness existed within these Ti-Zr-Nb-Ta alloys. In conjunction with their microscopic morphology and phase structure analysis, the amorphous films exhibited greater hardness versus the BCC-structured alloys. Compared to the crystalline films, the amorphous films contained a higher ZrTa content. The large atomic size difference in the amorphous films increased their structural disorder. The extensive lattice distortion inherent to the amorphous structures resulted in high dislocation migration resistance, which was the primary rationale for the enhanced hardness of the amorphous alloys.

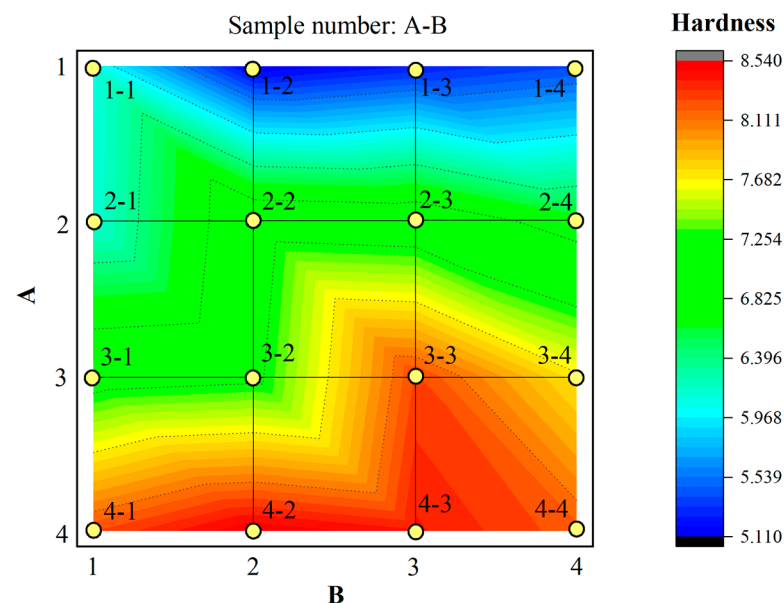


Figure 6. Trends in the indentation hardness of Ti-Zr-Nb-Ta alloys.

The Young's modulus of Ti-Zr-Nb-Ta alloys was also tested via nanoindentation. The measured Young's modulus of the films spanned 110 to 133 GPa, as presented in Figure 7. Notably, alloys 2-3 and 2-4 exhibited relatively high Young's modulus values, while the Young's modulus of the other alloys was at a relatively low level. Through compari-

son, it was discerned that Young's modulus trend did not correlate with the observed hardness changes.

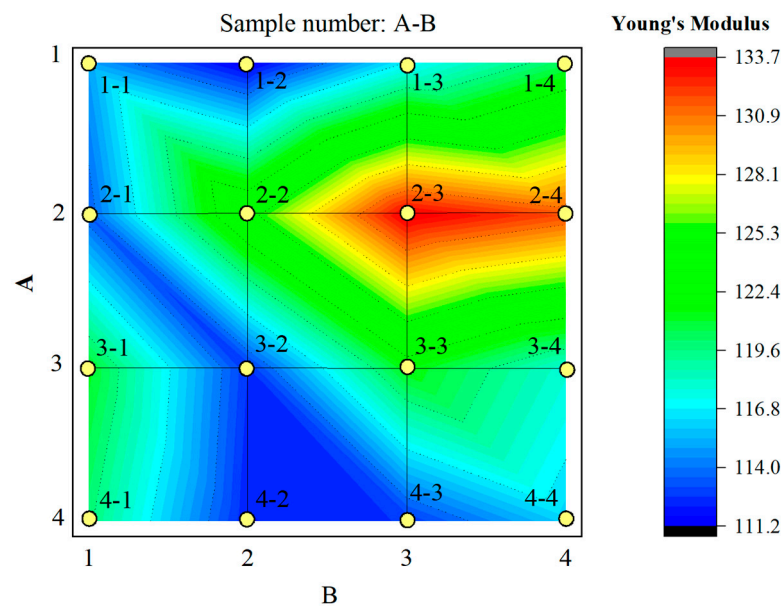


Figure 7. Trends in the Young's modulus of the Ti-Zr-Nb-Ta alloys.

Moreover, the cooling rate of films obtained via magnetron sputtering is higher than that of bulk alloy fabricated using a melting method, which induces a non-equilibrium state in films. In this case, the films generally show a semi-crystal structure or fine-grained structure, resulting in a significant increase in dislocation migration resistance. Hence, for a given composition, the hardness of films was typically greater than that of bulk alloys. Notably, with changes in alloy composition, the mechanical properties of both films and bulk alloys displayed consistent trends. This arose because several intrinsic physical parameters like atomic size mismatch, modulus mismatch, and valence electron concentration (VEC) solely depended on composition. Therefore, this combinatorial film library could feasibly guide the design of Ti-Zr-Nb-Ta bulk alloys. Concurrently, the synergistic design of MPEAs based on principles of VEC theory and average shear modulus mismatch has been proven to enable excellent biomedical MPEAs [22]. Briefly, integrating this combinatorial film library with a synergistic design philosophy for bulk MPEAs will expedite the development of superior biomedical alloys.

4. Discussions

The parallel preparation of Ti-Zr-Nb-Ta alloys was studied utilizing multi-target co-sputtering combined with physical masking. Sixteen specimens with different compositions were fabricated. Based on a preliminary investigation of this alloy, several issues were highlighted, as follows:

(1) The material library displayed extensive coverage across multi-principal component alloy compositions. Regarding component gradients, the elemental content decreased towards the periphery, with the deposition source at the center. Accordingly, the composition range of each component can be modulated by altering the relative position between the target material and substrate. Additionally, modifying the sputtering power of individual targets and adjusting the target-to-substrate distance can further tune the composition range of the material library.

(2) The sixteen Ti-Zr-Nb-Ta alloys exhibit two typical structures, including a single-BCC phase structure and an amorphous structure. Microstructural characterization revealed distinct morphological features associated with each phase structure. Specifically, the films with a BCC phase structure exhibited a rough surface morphology of nanocryst-

tals, while the films with an amorphous structure showed a relatively smooth surface morphology. Moreover, alloy films containing more ZrTa show larger lattice parameters, with the diffraction peaks shifting to the low angle of alloys. Accordingly, this combinatorial material library enabled rapid screening of the phase structure, microstructure, and lattice constant.

(3) The mechanical properties of multi-principal alloys were also examined utilizing the material library. The Young's modulus and nanoindentation hardness of the Ti-Zr-Nb-Ta alloys spanned 110 to 130 GPa and 5 to 8.5 GPa, respectively, exhibiting relatively high hardness and a low modulus. Contour mapping enabled clear visualization of the compositional dependence of the hardness and modulus, providing a platform to screen compositions for target mechanical properties.

(4) Overall, the Ti-Zr-Nb-Ta alloys exhibited a low modulus, and the constituent elements demonstrated biocompatibility. Compared to classic biomedical materials, such as Ti-6Al-4V alloy (with a Young's modulus of 110 GPa), CoCrMo alloy (with a Young's modulus of 230 GPa), and 316L SS (with a Young's modulus of 210 GPa), the Ti-Zr-Nb-Ta alloys spanned a Young's modulus range of 110–130 GPa. Therefore, the Ti-Zr-Nb-Ta alloys show potential for application in biomedical materials. This work provides a foundation that will enable the future screening and design of Ti-Zr-Nb-Ta biomedical alloys.

5. Conclusions

In summary, this work enables parallel fabrication of Ti-Zr-Nb-Ta, multi-principal element alloys with excellent mechanical performance, characterized by a low Young's modulus and high strength. Preliminary studies indicate the Ti-Zr-Nb-Ta system holds great potential as a biomedical material class. This high-throughput fabrication process pioneers a new paradigm for the parallel synthesis and screening of biomaterials. Moving forward, evaluating corrosion resistance, wear resistance, and fracture toughness should be key priorities. Ultimately, this combinatorial approach is expected to accelerate the discovery and optimization of MPEAs for next-generation biomedical applications.

Author Contributions: Conceptualization, X.Y.; Methodology, H.Q., X.Y. and S.G.; Investigation, H.Q.; Data Curation, H.Q.; Project administration, S.W.; Software, W.J.; Writing—original draft preparation, H.Q.; Writing—review and editing, H.Q. and X.Y.; Supervision, B.Z. All authors have read and agreed to the published version of the manuscript.

Funding: This research was funded by the Youth Fund Project of GRINM (No.66922309), the National Natural Science Foundation of China (No.52301220), and the Innovation Foundation of the GRIMAT Engineering Institute (No.57922201).

Institutional Review Board Statement: Not applicable.

Informed Consent Statement: Not applicable.

Data Availability Statement: Data available on request. The data presented in this study are available on request from the corresponding author. The data are not publicly available due to privacy or ethics.

Conflicts of Interest: The authors declare no conflict of interest.

References

1. George, E.P.; Raabe, D.; Ritchie, R.O. High-entropy alloys. *Nat. Rev. Mater.* **2019**, *4*, 515–534. [[CrossRef](#)]
2. Zhang, Y.; Zuo, T.T.; Tang, Z.; Gao, M.C.; Dahmen, K.A.; Liaw, P.K.; Lu, Z.P. Microstructures and properties of high-entropy alloys. *Prog. Mater. Sci.* **2014**, *61*, 1–93. [[CrossRef](#)]
3. Zhang, W.; Liaw, P.K.; Zhang, Y. Science and technology in high-entropy alloys. *Sci. China Mater.* **2018**, *61*, 2–22. [[CrossRef](#)]
4. He, J.Y.; Wang, H.; Huang, H.L.; Xu, X.D.; Chen, M.W.; Wu, Y.; Liu, X.J.; Nieh, T.G.; An, K.; Lu, Z.P. A precipitation-hardened high-entropy alloy with outstanding tensile properties. *Acta Mater.* **2016**, *102*, 187–196. [[CrossRef](#)]
5. Li, Z.; Pradeep, K.G.; Deng, Y.; Raabe, D.; Tسان, C.C. Metastable high-entropy dual-phase alloys overcome the strength–ductility trade-off. *Nature* **2016**, *534*, 227–230. [[CrossRef](#)] [[PubMed](#)]
6. Senkov, O.N.; Wilks, G.B.; Scott, J.M.; Miracle, D.B. Miracle, Mechanical properties of Nb₂₅Mo₂₅Ta₂₅W₂₅ and V₂₀Nb₂₀Mo₂₀Ta₂₀W₂₀ refractory high entropy alloys. *Intermetallics* **2011**, *19*, 698–706. [[CrossRef](#)]

7. Senkov, O.N.; Senkova, S.V.; Woodward, C.; Miracle, D.B. Low-density, refractory multi-principal element alloys of the Cr–Nb–Ti–V–Zr system: Microstructure and phase analysis. *Acta Mater.* **2013**, *61*, 1545–1557. [[CrossRef](#)]
8. Li, D.; Li, C.; Feng, T.; Zhang, Y.; Sha, G.; Lewandowski, J.J.; Liaw, P.K. High-entropy Al_{0.3}CoCrFeNi alloy fibers with high tensile strength and ductility at ambient and cryogenic temperatures. *Acta Mater.* **2017**, *123*, 285–294. [[CrossRef](#)]
9. Liu, J.; Guo, X.; Lin, Q.; He, Z.; An, X.; Li, L.; Liaw, P.K.; Liao, X.; Yu, L.; Lin, J.; et al. Excellent ductility and serration feature of metastable CoCrFeNi high-entropy alloy at extremely low temperatures. *Sci. China Mater.* **2019**, *62*, 853–863. [[CrossRef](#)]
10. Lee, C.; Chang, C.; Chen, Y.; Yeh, J.; Shih, H. Effect of the aluminium content of Al_xCrFe_{1.5}MnNi_{0.5} high-entropy alloys on the corrosion behaviour in aqueous environments. *Corros. Sci.* **2008**, *50*, 2053–2060. [[CrossRef](#)]
11. Fu, Y.; Li, J.; Luo, H.; Du, C.; Li, X. Recent advances on environmental corrosion behavior and mechanism of high-entropy alloys. *J. Mater. Sci. Technol.* **2021**, *80*, 217–233. [[CrossRef](#)]
12. Das, P.; Nandan, R.; Pandey, P.M. A review on corrosion properties of high entropy alloys fabricated by additive manufacturing. *Trans. Indian Inst. Met.* **2022**, *75*, 2465–2476. [[CrossRef](#)]
13. Yan, X.; Zhang, Y. Functional properties and promising applications of high entropy alloys. *Scr. Mater.* **2020**, *187*, 188–193. [[CrossRef](#)]
14. Cheng, Z.; Sun, J.; Gao, X.; Wang, Y.; Cui, J.; Wang, T.; Chang, H. Irradiation effects in high-entropy alloys and their applications. *J. Alloys Compd.* **2023**, *930*, 166768. [[CrossRef](#)]
15. Zhang, Z.; Armstrong, D.E.; Grant, P.S. The effects of irradiation on CrMnFeCoNi high-entropy alloy and its derivatives. *Prog. Mater. Sci.* **2022**, *123*, 100807. [[CrossRef](#)]
16. Zhang, Y.; Yan, X.; Ma, J.; Lu, Z.; Zhao, Y. Compositional gradient films constructed by sputtering in a multicomponent Ti–Al–(Cr, Fe, Ni) system. *J. Mater. Res.* **2018**, *33*, 3330–3338. [[CrossRef](#)]
17. Yan, X.-H.; Ma, J.; Zhang, Y. High-throughput screening for biomedical applications in a Ti–Zr–Nb alloy system through masking co-sputtering. *Sci. China Phys. Mech. Astron.* **2019**, *62*, 996111. [[CrossRef](#)]
18. Xing, Q.; Ma, J.; Wang, C.; Zhang, Y. High-throughput screening solar-thermal conversion films in a pseudobinary (Cr, Fe, V)–(Ta, W) system. *ACS Comb. Sci.* **2018**, *20*, 602–610. [[CrossRef](#)]
19. Dong, Y.G.; Chen, S.; Jia, N.N.; Zhang, Q.H.; Wang, L.; Xue, Y.F.; Jin, K. Microstructures and mechanical properties of Ta–Nb–Zr–Ti–Al refractory high entropy alloys with varying Ta/Ti ratios. *Tungsten* **2021**, *3*, 406–414. [[CrossRef](#)]
20. Lei, Z.; Liu, X.; Wu, Y.; Wang, H.; Jiang, S.; Wang, S.; Hui, X.; Wu, Y.; Gault, B.; Kontis, P.; et al. Enhanced strength and ductility in a high-entropy alloy via ordered oxygen complexes. *Nature* **2018**, *563*, 546–550. [[CrossRef](#)]
21. Ye, Y.; Lu, Z.; Nieh, T. Dislocation nucleation during nanoindentation in a body-centered cubic TiZrHfNb high-entropy alloy. *Scr. Mater.* **2017**, *130*, 64–68. [[CrossRef](#)]
22. Li, Z.; Lai, W.J.; Tong, X.; You, D.Q.; Li, W.; Wang, X.J. Design of TiZrNbTa multi-principal element alloys with outstanding mechanical properties and wear resistance. *Mater. Sci. Eng. A* **2022**, *845*, 143203. [[CrossRef](#)]
23. Zhang, Y.; Lu, Z.P.; Ma, S.G.; Liaw, P.K.; Tang, Z.; Cheng, Y.Q.; Gao, M.C. Guidelines in predicting phase formation of high-entropy alloys. *MRS Commun.* **2014**, *4*, 57–62. [[CrossRef](#)]

Disclaimer/Publisher’s Note: The statements, opinions and data contained in all publications are solely those of the individual author(s) and contributor(s) and not of MDPI and/or the editor(s). MDPI and/or the editor(s) disclaim responsibility for any injury to people or property resulting from any ideas, methods, instructions or products referred to in the content.